CrossMark

ORIGINAL PAPER

Quantify patient-specific coronary material property and its impact on stress/strain calculations using in vivo IVUS data and 3D FSI models: a pilot study

Xiaoya Guo[1] · Jian Zhu[2] · Akiko Maehara[3] · David Monoly[4] · Habib Samady[4] ·
Liang Wang[5] · Kristen L. Billiar[6] · Jie Zheng[7] · Chun Yang[8] · Gary S. Mintz[3] ·
Don P. Giddens[4,9] · Dalin Tang[1,5]

Abstract Computational models have been used to calculate plaque stress and strain for plaque progression and rupture investigations. An intravascular ultrasound (IVUS)-based modeling approach is proposed to quantify in vivo vessel material properties for more accurate stress/strain calculations. In vivo Cine IVUS and VH-IVUS coronary plaque data were acquired from one patient with informed consent obtained. Cine IVUS data and 3D thin-slice models with axial stretch were used to determine patient-specific vessel material properties. Twenty full 3D fluid–structure interaction models with ex vivo and in vivo material properties and various axial and circumferential shrink combinations were constructed to investigate the material stiffness impact on stress/strain calculations. The approximate circumferential Young's modulus over stretch ratio interval [1.0, 1.1] for an ex vivo human plaque sample and two slices (S6 and S18) from our IVUS data were 1631, 641, and 346 kPa, respectively. Average lumen stress/strain values from models using ex vivo, S6 and S18 materials with 5 % axial shrink and proper circumferential shrink were 72.76, 81.37, 101.84 kPa and 0.0668, 0.1046, and 0.1489, respectively. The average cap strain values from S18 material models were 150–180 % higher than those from the ex vivo material models. The corresponding percentages for the average cap stress values were 50–75 %. Dropping axial and circumferential shrink consideration led to stress and strain over-estimations. In vivo vessel material properties may be considerably softer than those from ex vivo data. Material stiffness variations may cause 50–75 % stress and 150–180 % strain variations.

Keywords Vulnerable plaque · Artery material properties · Patient-specific model · FSI · IVUS

Xiaoya Guo and Jian Zhu have contributed equally to this work.

✉ Dalin Tang
  dtang@wpi.edu

[1] Department of Mathematics, Southeast University, Nanjing 210096, China

[2] Department of Cardiology, Zhongda Hospital, Southeast University, Nanjing 210009, China

[3] The Cardiovascular Research Foundation, Columbia University, New York, NY 10022, USA

[4] Department of Medicine, Emory University School of Medicine, Atlanta, GA 30307, USA

[5] Mathematical Sciences Department, Worcester Polytechnic Institute, Worcester, MA 01609, USA

[6] Department of Biomedical Engineering, Worcester Polytechnic Institute, Worcester, MA 01609, USA

[7] Mallinckrodt Institute of Radiology, Washington University, St. Louis, MO 63110, USA

[8] Network Technology Research Institute, China United Network Communications Co., Ltd., Beijing, China

[9] The Wallace H. Coulter Department of Biomedical Engineering, Georgia Institute of Technology, Atlanta, GA 30332, USA

1 Introduction

Cardiovascular diseases (CVD), especially acute coronary syndromes, are closely associated with atherosclerotic plaque progression and rupture. Atherosclerotic plaque progression and rupture are believed to be related to morphological factors, plaque components, material properties, and mechanical stress/strain conditions (Bluestein et al. 2008; Cardoso and Weinbaum 2014; Fleg et al. 2012; Fuster 1998; Friedman et al. 2010; Samady et al. 2011; Stary et al. 1995; Stone et al. 2012; Tang et al. 2008, 2009, 2014). Computational models have been used as a powerful tool to perform

mechanical analysis and identify risk factors and mechanisms which may be associated with plaque progression and rupture (Friedman et al. 2010; Tang et al. 2014). Modeling results and stress/strain predictions are influenced by many complex factors including plaque morphology, components, material properties, and modeling assumptions (Tang et al. 2014). Since patient-specific vessel material properties are in general not available, most current models used material properties from existing literature (Humphrey 2002; Holzapfel et al. 2004). It is desirable to have patient-specific material properties in computational models for more accurate stress/strain calculations.

Human coronary material properties are difficult to obtain because it is hard to get human coronary tissue samples. Quantification of in vivo coronary material properties of human tissues is even harder. Extensive efforts have been made by several research groups to quantify mechanical material properties of atherosclerotic arteries and their impacts on stress/strain predictions. Holzapfel et al. (2002, 2004) investigated layer- and direction-dependent ultimate tensile stress and stretch ratio of human atherosclerotic iliac arteries and showed that anisotropic and highly nonlinear tissue properties were observed as well as interspecimen differences (Holzapfel et al. 2002, 2004). The adventitia demonstrated the highest strength and fibrous cap in circumferential direction showed low fracture stress. Different layers displayed different direction-dependent mechanical behaviors which are crucial for realistic computational models and accurate stress/strain predictions (Holzapfel 2000; Holzapfel et al. 2000, 2002, 2004). Pandit et al. (2005) determined biaxial elastic material properties of porcine coronary media and adventitia using specimen from the slaughterhouse. Barrett et al. (2009) used 8 human carotid plaque samples and an indention method to determine fibrous cap material properties. Teng et al. (2009) performed uniaxial tests on 73 axial and circumferential oriented adventitia, media and intact specimens prepared from 6 human carotid arteries. Their results showed that the mean axial and circumferential ultimate strength of the media group were 519 ± 270 kPa and 1230 ± 533 kPa, respectively, while the corresponding ultimate strength for the adventitia was 1996 ± 867 kPa and 1802 ± 703 kPa, respectively. Kural et al. (2012) performed biaxial mechanical testing using 8 human coronary plaque samples and 5 carotid plaque samples. Both longitudinal and circumferential stress versus strain plots were provided. Their results indicated that coronary arteries were clearly stiffer and less extensible than the carotid arteries in both directions. The mean opening angles for coronary and carotid samples were 120° and 63.5°, respectively. Liu et al. (2012) introduced a finite element approach based on in vivo MRI Cine data to determine human carotid material properties. Their results from 12 patients showed that material stiffness measured by the effective Young's

modulus (YM) varied from 137 (soft), 431 (median), to 1435 kPa (stiff), respectively. Karimi et al. (2015) obtained uniaxial mechanical properties of healthy and atherosclerotic human coronary arteries from 22 human coronary arteries. Teng et al. (2014) reported uniaxial mechanical testing of human carotid plaque component tissues from 21 human carotid plaque samples. The median values of incremental YM of media, fibrous cap (FC), lipid and intraplaque hemorrhage/thrombus (IPH/T) at $\lambda = 1$ were 290.1, 244.5, 104.4, 52.9, respectively; they increase to 1019.5, 817.4, 220.7 and 176.9 at $\lambda = 1.1$; and 4302.7, 3335.0, 533.4 and 268.8 at $\lambda = 1.15$ (unit: kPa; λ: stretch ratio), reflecting the nonlinearity of the material properties. Nieuwstadt et al. (2015) investigated the feasibility of estimating carotid plaque component elasticity constants using ultrasound elastography, MRI, and inverse finite element analysis. The intima elasticity constant C_1 (160 kPa scenario) was estimated as 125.8 ± 19.4 kPa (reader1) and 128.9 ± 24.8 kPa (reader2). The lipid-rich necrotic core C_1 (5 kPa) was estimated as 5.6 ± 2.0 kPa (reader1) and 8.5 ± 4.5 kPa (reader2). Chai et al. (2015) investigated local anisotropic mechanical properties of human carotid atherosclerotic plaques by micro-indentation and inverse finite element analysis. Walsh et al. (2014) provided an excellent review of 9 studies of uniaxial mechanical testing of atherosclerotic plaque tissues.

In addition to material properties and issues covered above, another important issue for models based on in vivo data is that the determination of a shrinkage rate (axial and circumferential shrinkage for 3D models) needed to shrink the vessel in vivo geometry to its zero-pressure shape. Tang et al. (2009) and Yang et al. (2009) introduced a shrink-stretch process to (a) shrink the vessel both axially and circumferentially to obtain the "no-load" shape as the numerical starting geometry; and (b) stretch and pressurize the vessel to recover its in vivo shape under pressure and stretch conditions (Tang et al. 2008, 2009; Yang et al. 2007, 2009). Speelman et al. and Gee et al. also demonstrated the necessity and importance of the pre-shrink process by using their in vivo computed tomography (CT)-based abdominal aortic aneurysm simulations (Speelman et al. 2011; Gee et al. 2009).

In this paper, in vivo Cine intravascular ultrasound (IVUS) data and 3D VH-IVUS (Virtual Histology IVUS) data were acquired to quantify patient-specific coronary material properties in vivo and to construct 3D plaque models for stress/strain calculations. Patient-specific and slice-specific circumferential shrinkage rates needed to obtain the vessel no-load geometry were also determined in the material parameters calculation process. Twenty 3D FSI models were constructed from the IVUS data with 4 different material properties and various combinations of axial and circumferential shrinkages to investigate the impacts of plaque material properties and axial and circumferential shrinkages on stress/strain calculations.

2 Data, models and methods

2.1 In vivo IVUS and VH-IVUS data acquisition

In vivo grayscale IVUS and VH-IVUS data of human coronary were acquired from one patient (male, age 58) at Zhongda Hospital, Southeast University, Nanjing, China, with informed consent obtained. IVUS data acquisition followed standard procedure described in (Yang et al. 2009). A 20MHz, 2.9F phased-array transducer catheter (Eagle Eye Platinum, Volcano Corp, Rancho Cordova, CA) was used. The original grayscale of IVUS image had an axial resolution of 150–200 µm and a lateral resolution of 150–300 µm (Mintz et al. 2001). The VH-IVUS (IVUS Virtual Histology, Volcano S5, Volcano Corp, Rancho Cordova, CA) was obtained by using autoregressive models to provide 4 classified tissue components (Nair et al. 2002). The segmented VH-IVUS contour data for model construction have 20 µm pixel resolution given by the segmentation software. Figure 1 shows two VH-IVUS slice samples showing the four tissue types by color: necrotic core in red, calcium in white, fibrous in dark green and fibro-fatty in light green. The distribution of each type tissue can be seen in VH-IVUS slices. Fibrous and Fibro-Fatty were considered as having the same material properties as vessel tissue and were combined in our image data pre-processing. There was very little calcium in this sample and was ignored for simplicity. Original VH-IVUS segmented data contained many tiny blocks of tissue components and many components of irregular shapes difficult for mesh generation. The image data pre-processing consisted of filtering out very small items, merging cluster of small components to larger ones, 2D smoothing, and 3D smoothing. After pre-processing, our plaque model ended up with a few plaque components with manageable number and shape. Our final model in this paper had two types of tissues: vessel tissue and necrotic core (lipid). Forty-four VH-IVUS slices were selected for model construction.

To obtain Cine IVUS data which would be used to determine vessel material parameter values, the catheter paused 5–10 s at 5 locations during its pull-out. When the catheter was paused, IVUS images of the vessel at the fixed locations with diameter variations were recorded. The locations of the catheter were recorded by angiography (Allura Xper FD10 System, Philips, Bothel, WA). According to the quality of images, two locations (S6, S18) were selected to make thin-slice models. Figure 1 shows the stacked contours of the 44- slice VH-IVUS dataset and two selected slices from Cine IVUS with maximum and minimum lumen circumferences, respectively. Segmented grayscale IVUS Cine slice contained only lumen contour and wall contour. It should be noted that VH-IVUS and Cine IVUS contours appear slight differently because different segmentation methods were used.
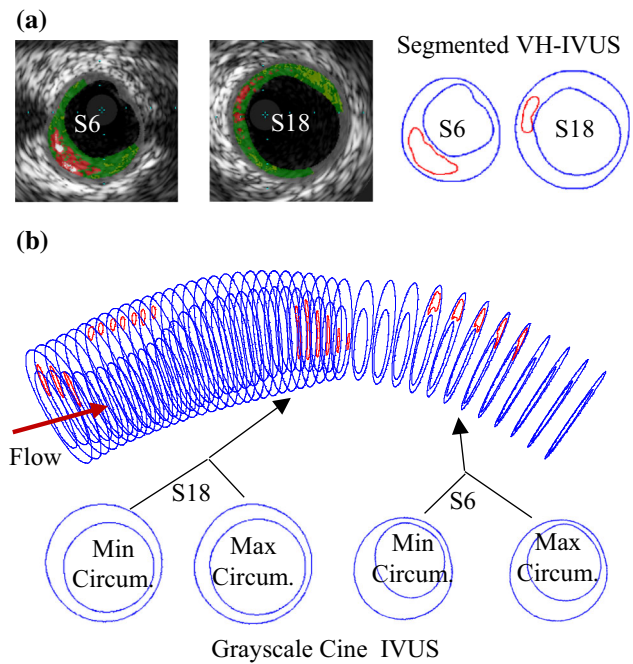

Fig. 1 Selected VH-IVUS slices, segmented contour plots, 3D vessel geometry with registered Cine IVUS slices. Colors used in IVUS-VH: *Red* necrotic core, *White* dense calcium, *Dark Green* Fibrous, *Light Green* Fibro-Fatty

2.2 The Mooney–Rivlin material model and 3D thin-slice model

Three-dimensional thin-slice models and Cine IVUS data were used to determine vessel material properties from the 2 selected slices (S6 and S18). The thin-slice models were made by adding a thin slice thickness to the 2D slices so that the models became 3D and axial stretch could be applied, mimicking the axial stretch in full 3D models. Axial shrinkage was set at 5 % in our models because atherosclerotic vessels were stiffer than healthy vessels. The governing equations and boundary conditions of the structure model can be found in our previous publication (Yang et al. 2009). The anisotropic Mooney–Rivlin model was used for the vessel tissue. Its strain energy density function is:

$$
\begin{aligned}
W = {} & c_1(I_1 - 3) + c_2(I_2 - 3) \\
& + D_1[\exp(D_2(I_1 - 3)) - 1] \\
& + (K_1/K_2)\exp[K_2(I_4 - 1)^2 - 1],
\end{aligned} \tag{1}
$$

$$
\begin{aligned}
I_1 &= \sum C_{ii}, \quad I_2 \\
&= 1/2[I_1^2 - C_{ij}C_{ij}],
\end{aligned} \tag{2}
$$

where I_1 and I_2 are the first and second invariants of right Cauchy–Green deformation tensor $\mathbf{C}$ defined as $C = [C_{ij}] = \mathbf{X}^{\mathrm{T}}\mathbf{X}$, $\mathbf{X} = [X_{ij}] = [\partial x_i / \partial a_j]$, (x_i) is current position, (a_i) is original position, $I_4 = C_{ij}(\mathbf{n}_c)_i(\mathbf{n}_c)_j$, $\mathbf{n}_c$ is the unit vector

in the circumferential direction of the vessel, c_1, c_2, D_1, D_2, K_1 and K_2 are material parameters (Holzapfel et al. 2000; Yang et al. 2009) whose values are to be determined using in vivo IVUS data. The VH-IVUS slices (slice 6, 18) registered with Cine IVUS were used to make thin-slice models. The lumen circumference variations from Cine IVUS were used to determine material parameter values using an iterative procedure given in Sect. 2.3. Pressure boundary conditions were imposed on the lumen surface using patient's arm pressures. The external pressure was set to zero.

Plaque components (specifically, the necrotic lipid core in this study) were assumed isotropic, and the isotropic Mooney–Rivlin material model was used to describe their material properties.

$$W_{\text{iso}} = c_1(I_1 - 3)$$
$$+ c_2(I_2 - 3) + D_1[\exp(D_2(I_1 - 3)) - 1], \qquad (3)$$

The material constants for lipid material from existing literature were used in this paper (Yang et al. 2009): $c_1 = 0.5$ kPa, $c_2 = 0$, $D_1 = 0.5$ kPa and $D_1 = 1.5$.

2.3 The iterative scheme to determine patient-specific material parameter values

In our earlier effort to quantify coronary plaque material properties, biaxial testing was performed using eight coronary arteries from four cadavers (age: 50–81) and a two-step square-least method was conducted to fit our experimental data for the Mooney–Rivlin material model to get the material constants (Kural et al. 2012). The parameter values $c_1 = -1312.9$ kPa, $c_2 = 114.7$ kPa, $D_1 = 629.7$ kPa, $D_2 = 2.0$, $K_1 = 35.9$ kPa, $K_2 = 23.5$ obtained from one plaque sample were used as the initial guess in our iterative procedure in this paper. To determine in vivo plaque material properties, for each thin-slice model, an iterative procedure was used to adjust the parameter values in the Mooney–Rivlin model and the circumferential shrinkage rate to match both maximum and minimum Cine IVUS lumen circumferences corresponding to systolic and diastolic pressures, respectively. Since we have only two data points to work with (maximum and minimum lumen circumferences corresponding to maximum and minimum arm pressure), only two quantities can be determined in theory. That means choices of material parameter values would not be unique. We chose to determine one material ratio k and circumferential shrinkage. In our iteration process, we fixed $D_2 = 2.0$ and $K_2 = 23.5$ and adjusted other material parameters proportionally to the initial guess, that is, $c_1 = k * (-1312.9)$ kPa, $c_2 = k * 114.7$ kPa, $D_1 = k * 629.7$ kPa, $K_1 = k * 35.9$ kPa. Figure 2 gives a diagram for the iteration process. The initial lumen shrinkage rate S1

was set to be 5 %. At each iteration step, the lumen contour would be shrunk by S1. The slice outer-boundary shrinkage rate was determined using conservation of the vessel volume. Material parameter values as a proportion to the initial guess were adjusted so that the lumen circumference matched minimum IVUS lumen circumference at diastole pressure. Then the lumen circumference under maximum pressure was obtained and used to compare with the maximum Cine IVUS lumen circumference. If not matched (i.e., error > tolerance), then S1 would be adjusted and the iteration continued. The iterative procedure was set to stop if the relative changes of the shrinkage and parameter values were <0.01 (1 %). The parameter values determined for S6 and S18 are reported in Sect. 3. Figure 3a gives plots of stress/stretch curves for the three materials from the anisotropic Mooney–Rivlin models, for both axial and circumferential stress curves.

2.4 3D FSI models to quantify impact of plaque material properties on stress/strain calculations

3D models with full fluid–structure interactions were constructed using the 44-slice IVUS data set to quantify the impact of plaque material properties on stress/strain calculations. Details of the FSI model can be found in our previous publications (Yang et al. 2009). Figure 3b gives the pressure conditions imposed at the inlet and outlet of the vessel with arm systole and diastole pressure from the patient used as the maximum and minimum values of the profile. For models based on in vivo morphology, we have demonstrated the importance of including axial and circumferential shrinkage in the model construction process (Huang et al. 2009). Four different materials were used for vessel material properties in our models: Material 1 (Mat-1): the ex vivo material; Material 2 (Mat-2): parameter values obtained from S6 (note: this material was used for the entire vessel, same for the next one); Material 3 (Mat-3): parameter values obtained from S18; Material 4 (Mat-4): half vessel using material parameter values from S6, the other half using S18. Five groups of models were constructed using the 4 materials: Group 1 has 5 % axial shrink and proper circumferential shrinkage so that the vessel recovers its in vivo shape after axial stretch and pressurization. Group 2 has 5 % axial shrink and a fixed circumferential shrinkage (5.7 %) for all 4 materials. Group 3 has no axial shrink, but proper circumferential shrinkages were applied so that the vessel recovered its in vivo shape after pressurization. Group 4 has no axial shrink and a fixed 5.7 % circumferential shrinkage. Group 5 has no axial shrink and no circumferential shrinkage. Table 1 lists all the 20 models with their modeling assumptions. The models were solved to find out the influence of material properties and the axial and circumferential shrinkage on stress/strain calculations.

Fig. 2 Diagram for the iteration procedure to determine material parameter values
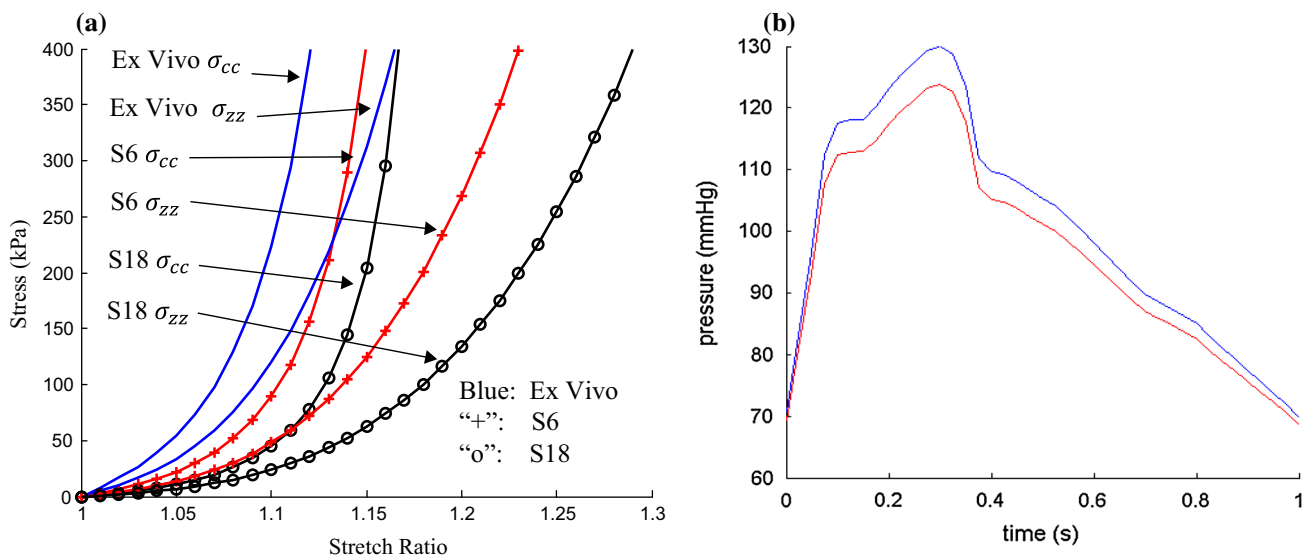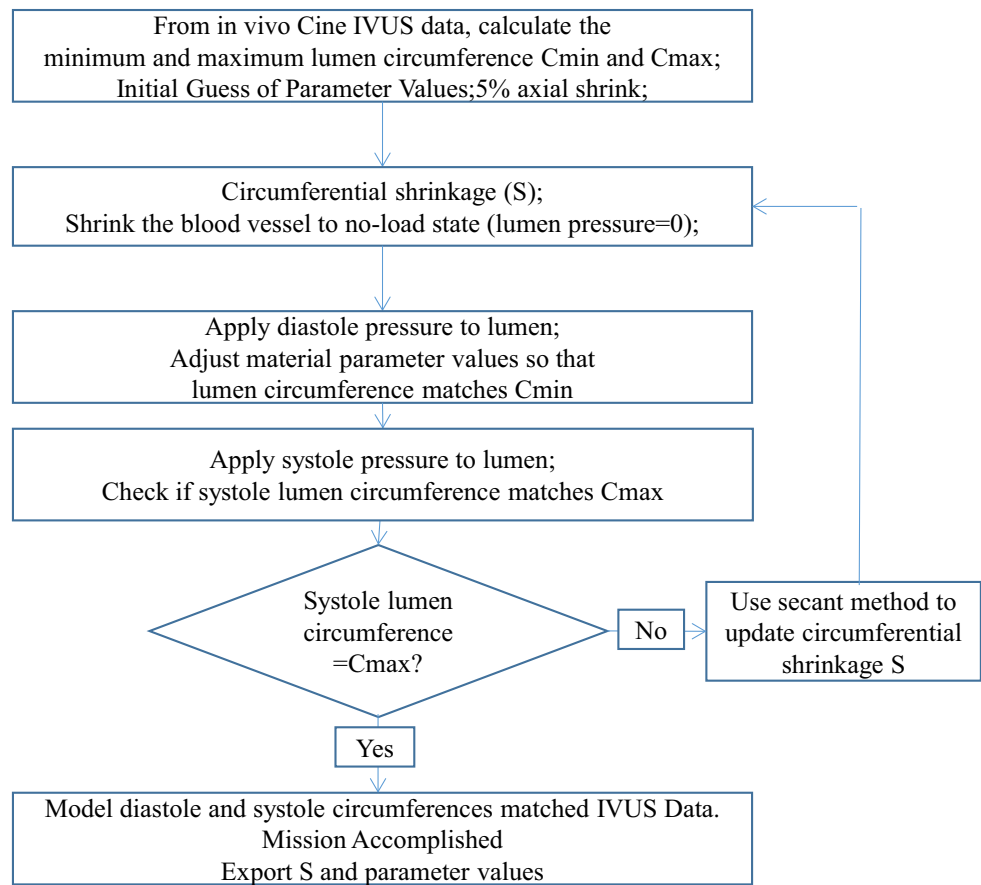
From in vivo Cine IVUS data, calculate the minimum and maximum lumen circumference Cmin and Cmax; Initial Guess of Parameter Values; 5% axial shrink;

↓

Circumferential shrinkage (S); Shrink the blood vessel to no-load state (lumen pressure=0);

↓

Apply diastole pressure to lumen; Adjust material parameter values so that lumen circumference matches Cmin

↓

Apply systole pressure to lumen; Check if systole lumen circumference matches Cmax

↓

Systole lumen circumference =Cmax? → No → Use secant method to update circumferential shrinkage S

↓ Yes

Model diastole and systole circumferences matched IVUS Data. Mission Accomplished Export S and parameter values

Fig. 3 Stress–stretch curves from the Mooney–Rivlin models for the ex vivo, S6 and S18 materials and pressure conditions used in the FSI models

2.5 Solution procedures and model comparisons

The models were solved by a commercial finite element software ADINA (Adina R & D, Watertown, MA, USA) following established procedures (Yang et al. 2009; Wang et al. 2015). Mesh analysis was performed by refining mesh density by 10 % until changes of solutions became <2 %. Three cardiac cycles were simulated in our computational models, and the solution in the third period was taken as the final result. Average stress, strain and flow shear stress on the

Table 1 Five groups 20 models with their associated material, axial and circumferential shrinkages

Group	Model	Material	Axial shrink (%)	Circumferential shrink
Group 1 5 % axial shrink adjusted C-shrink	M1-1	ExVivo	5	0.2 %
	M1-2	S6	5	4.6 %
	M1-3	S18	5	6.1 %
	M1-4	S6+S18	5	5 %, 4.8 %
Group 2 5 % axial shrink fixed C-shrink	M2-1	Ex Vivo	5	5.7 %
	M2-2	S6	5	5.7 %
	M2-3	S18	5	5.7 %
	M2-4	S6+S18	5	5.7 %
Group 3 0 % axial shrink adjusted C-shrink	M3-1	Ex Vivo	0	3 %
	M3-2	S6	0	6.3 %
	M3-3	S18	0	7.4 %
	M3-4	S6+S18	0	6.3 %, 6 %
Group 4 0 % axial shrink, fixed C-shrink	M4-1	Ex Vivo	0	5.7 %
	M4-2	S6	0	5.7 %
	M4-3	S18	0	5.7 %
	M4-4	S6+S18	0	5.7 %
Group 5 no axial shrink no C-shrink	M5-1	Ex Vivo	0	No
	M5-2	S6	0	No
	M5-3	S18	0	No
	M5-4	S6+S18	0	No

lumen and all the cap nodes covering the lipid-rich pool were recorded for comparison. To be clear, since stress and strain are tensors, maximum principal stress, maximum principal strain and maximum principal flow shear stress were taken as the scalar representatives of stress, strain and flow shear stress to present our results, respectively.

3 Results

3.1 Material parameter values determined from in vivo Cine IVUS data

Table 2 lists the parameter values for the Mooney–Rivlin models from one ex vivo coronary plaque sample and the two slices from our patient IVUS Cine data. Stress/stretch plots for the three materials from the anisotropic Mooney–Rivlin models were given by Fig. 3a, for both axial and circumferential stress curves. For easy comparison, approximate Young's Modulus (YM) values for all 6 curves on the interval [1.0, 1.1] were obtained using the least squares method. Using the softest material (S18) as the base, the circumferential YM value (YM_c) from S6 was 641 kPa, about 185 % of that from S18 (346 kPa). The ex vivo plaque sample YM_c value was 1631, about 470 % of that of S18.

3.2 Softer in vivo vessel material properties led to higher plaque stress and strain

Figure 4 presents the stress, strain, flow shear stress (FSS), and flow velocity plots from the 4 models

M1-1 to M1-4 on a sagittal cut to show the model differences and impact of vessel material properties. It also serves the purpose of showing basic 3D FSI solution features. Since locations of maximum stress and strain may change, it is also meaningful to compare models using their mean values. Table 3 provides average lumen and cap stress, strain and FSS values from M1 and M2 models. Figure 5 gives the average value bar chart plots from M1 and M2 models showing model differences. Among the 4 models in M1 group, average lumen stress and strain values from M1-3 (soft in vivo material from S18) were 40 and 123 % higher than those from M1-1 (ex vivo material). Average cap stress and strain values from M1-3 (soft S18 material) were 52 and 148 % higher than those from M1-1 (ex vivo material). The differences in fluid among the 4 models were modest (<5 %).

It is worth mentioning that different circumferential shrinkages were needed for the 4 M1 models to recover in vivo shape after stretching and pressurization. M2 models used a fixed 5.7 % circumferential shrinkage for all 4 mod-

Table 2 Material parameters in the Mooney–Rivlin model and their approximate Young's modulus on stretch ratio interval [1.0, 1.1] for an ex vivo human plaque sample and two slices (S6 and S18) from our IVUS data

Material	C_1 (kPa)	C_2 (kPa)	D_1 (kPa)	D_2	K_1 (kPa)	K_2	YM_c (kPa)	YM_a (kPa)
Mt 1: Ex vivo Biaxial	−1312.9	114.7	629.7	2.0	35.9	23.5	1631	938
Mt 2: In Vivo S6	−515.6	45.05	247.3	2.0	14.10	23.5	641	366
Mt 3: In Vivo S18	−278.7	24.35	133.7	2.0	7.62	23.5	346	198

YM_c: Young's modulus in circumferential direction; YM_a: Young's modulus in axial direction
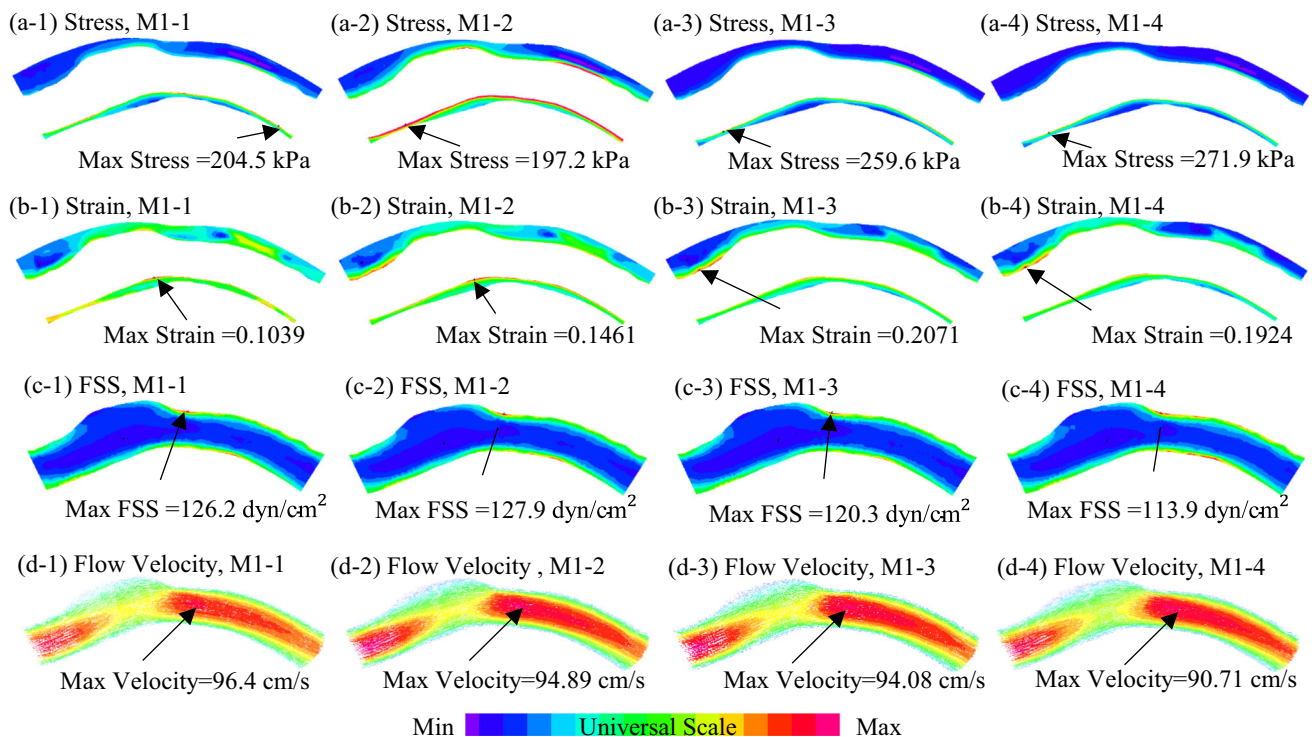
Fig. 4 Plaque stress, strain, flow shear stress (FSS) and velocity plots from the 4 M1 models showing solution behaviors and model differences. M1 models: 5 % axial shrink, adjusted circumferential shrinkage

Table 3 Softer vessel material properties from in vivo Cine IVUS data led to higher plaque stress and strain

Model	Axial shrinkage	Circum-shrinkage	Ave. lumen stress	Ave. lumen strain	Ave. cap stress	Ave. cap strain	Ave lumen FSS	Ave cap FSS
M1-1	5 %	0.2 %	72.76	0.0668	68.15	0.0626	52.35	56.44
M1-2		4.6 %	81.37	0.1046	81.84	0.1065	52.05	56.47
M1-3		6.1 %	101.84	0.1489	103.58	0.1553	50.76	55.28
M1-4		5 %, 4.8 %	94.27	0.1273	94.43	0.1297	50.40	55.20
M2-1	5 %	5.7 %	66.48	0.0654	60.71	0.0605	53.74	57.96
M2-2			80.26	0.1042	79.60	0.1058	52.07	55.90
M2-3			103.21	0.1494	103.80	0.1557	50.66	54.41
M2-4			93.51	0.1271	92.51	0.1293	50.86	55.04

M1 models have 5 % axial shrink with 4 different circumferential shrink adjusted to fit in vivo morphology. M2 models have 5 % axial shrink with the same 5.7 % circumferential shrink (therefore, M2 models did not fit in vivo morphology when loaded). Plaque stress and strain used maximum principal stress and strain as their scalar representative values. FSS used the maximum principal flow shear stress as its representative value

els to demonstrate the differences. The differences for the ex vivo material model (M1-1 vs. M2-1) were most noticeable with cap stress from M2-1 (60.71 kPa) 12.2 % lower than that from M1-1 (68.15 kPa). M2-2, M2-3, and M2-4 had very little difference compared to the corresponding M1 models. With the fixed circumferential 5.7 % shrink, average lumen stress and strain values from M2-3 (soft S18 material) were 55 and 128 % higher than those from M2-1 (ex vivo material). Average cap stress and strain values from M2-3 (soft S18 material) were 71 and 157 % higher than those from

M2-1 (ex vivo material). The differences caused by material property changes increased slightly compared to the M1 group.

3.3 Material impact on models without axial stretch

Table 4 provides average lumen and cap stress, strain and FSS values from M3 and M4 models, all with 0 % axial shrinkage, but keeping circumferential shrink. Figure 6 gives bar charts of average cap stress and strain from M1-3, M3-3,
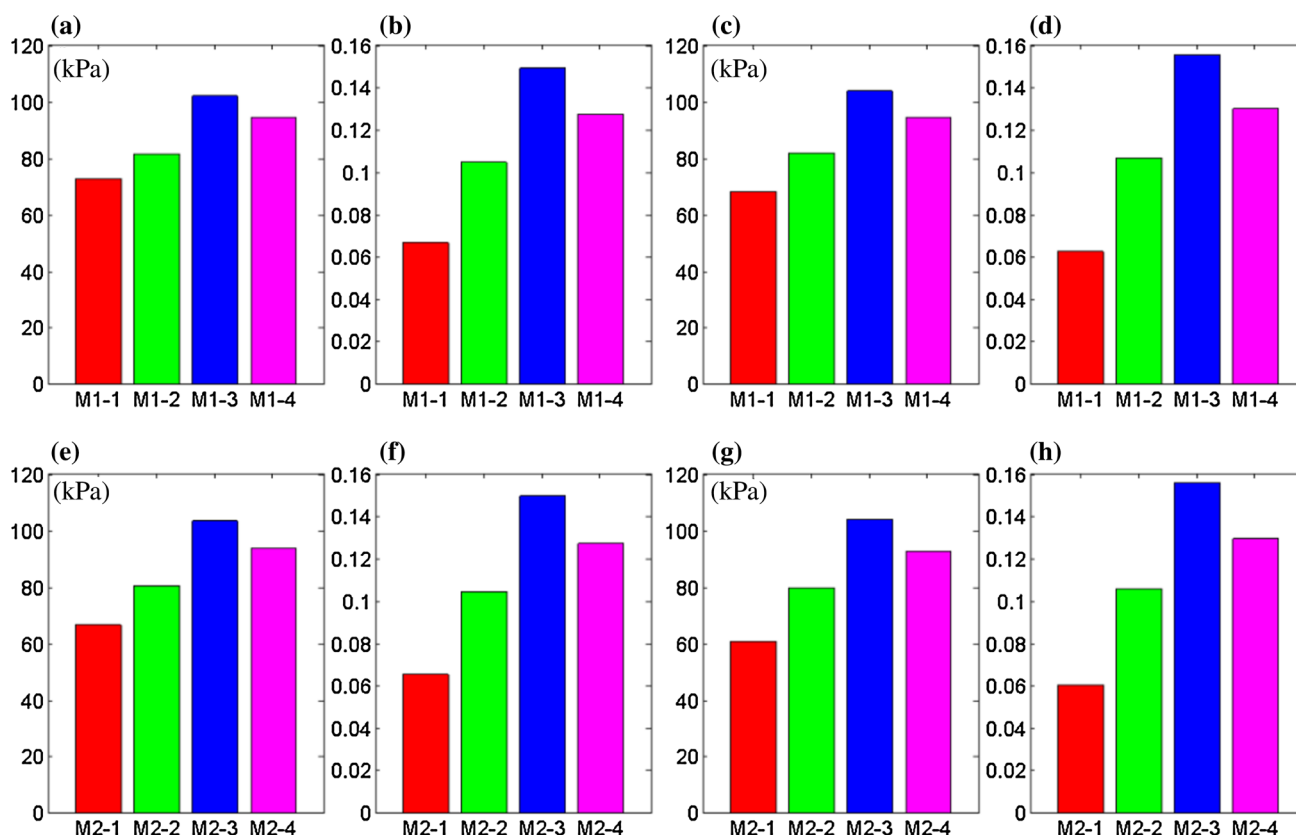
Fig. 5 Bar chart plots of average lumen and cap stress and strain values from M1 and M2 models showing easy comparisons. *Red* ex vivo material, *Green* stiffer in vivo material (from S6), *Blue* soft in vivo material (from S18), *Purple* half S6, and half S18

Table 4 Average lumen and cap stress, strain and flow shear stress (FSS) values from models with 0 % axial shrinkage and 3 sets of circumferential shrinkages showing combined impact of axial shrinkage and material properties on stress and strain calculations

Model	Axial shrinkage	Circum-shrinkage	Ave. lumen stress	Ave. lumen strain	Ave. cap stress	Ave. cap strain	Ave lumen FSS	Ave cap FSS
M3-1	0 %	3 %	71.35	0.0744	71.88	0.0797	50.94	56.03
M3-2		6.3 %	85.92	0.1214	85.73	0.1291	49.72	54.09
M3-3		7.4 %	106.68	0.1614	104.35	0.1712	48.61	53.28
M3-4		6.3 %, 6 %	97.08	0.1377	93.94	0.1441	48.69	53.76
M4-1	0 %	5.7 %	67.44	0.0728	67.75	0.0778	51.02	55.53
M4-2			86.84	0.1217	86.72	0.1295	49.34	53.55
M4-3			109.54	0.1621	107.47	0.1721	48.00	52.14
M4-4			97.70	0.1379	94.59	0.1443	48.35	52.84

M4-3 (soft in vivo material) and M1-1, M3-1, M4-1 (ex vivo material) showing clear comparisons. Without axial shrink, the average stress and strain values from M3 and M4 models were higher than those from M1 and M2 models. For example, average lumen stress and strain values from M4-3 (soft in vivo material) were 4.7 and 8.8 % higher than those from M1-3, respectively. Within the same group, average lumen stress and strain values from M4-3 were 62 and 123 % higher than those from M4-1 showing that material stiffness differ-

ence had greater impact on stress calculations with 0 % axial shrink.

3.4 Material impact on stress and strain calculations for models without axial and circumferential shrinkages

We constructed M5 models with 4 different material properties and 0 % axial and 0 % circumferential shrinkages. Average lumen and cap stress, strain and FSS values from
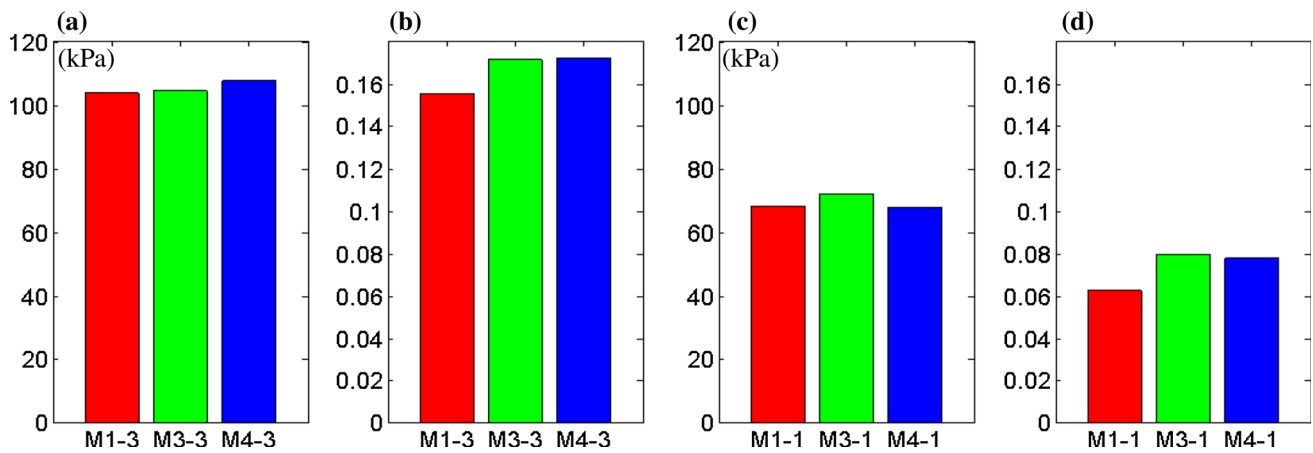
Fig. 6 Bar chart plots of average cap stress and strain values from M1, M3 and M4 models showing impact of axial shrink on stress/strain calculations. *Red* M1 models, 5 % axial shrink, adjusted circumferential shrink, *Green* M3 models, 0 % axial shrink, adjusted circumferential shrink, *Blue* M4 models, 0 % axial shrink, fixed 5.7 % circumferential shrink

Table 5 Average lumen and cap stress, strain and flow shear stress (FSS) values from models with 0 % axial shrinkage and 0 % circumferential shrinkage

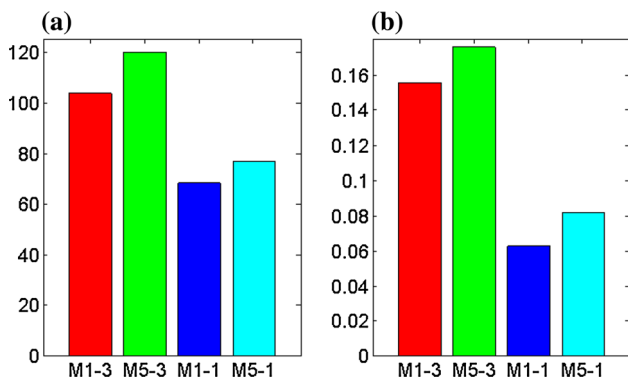| Model	Axial shrinkage	Circum-shrinkage	Ave. lumen stress	Ave. lumen strain	Ave. cap stress	Ave. cap strain	Ave lumen FSS	Ave cap FSS
M5-1	0 %	0 %	76.14	0.0763	76.75	0.0817	50.33	54.95
M5-2			96.73	0.1247	97.41	0.1332	48.63	53.00
M5-3			120.45	0.1645	119.82	0.1754	47.27	51.54
M5-4			108.18	0.1413	105.87	0.1478	47.62	52.15

Fig. 7 Bar chart plots of average cap stress and strain values from selected M1 and M5 models showing impact of dropping both axial and circumferential shrink. *Red* M1-3, *Orange* M5-3, *Blue* M1-1, *Light Blue* M5-1

M5 models are given in Table 5. Figure 7 gives bar chart plots of average cap stress and strain from M1-3, M5-3 (soft in vivo material) and M1-1, M5-1 (ex vivo material) showing their comparisons. Without circumferential shrinkage, the vessel over-expanded and exceeded its in vivo dimension under pressure. With 0 % axial shrink (which means 0 % axial stretch), the vessel would expand more leading to even greater stress/strain calculation errors. Our results indicated that average cap stress and strain values from M5-3 (soft in vivo material, no axial and circumferential shrink) were 16 % and 13 % higher than those from M1-3 (soft in vivo material, with 5 % axial and 6.1 % circumferential shrink). Within M5 models, average cap stress and strain values from M5-3 were 56 and 115 % higher than those from M5-1. Average lumen stress and strain comparisons gave similar results.

Figure 8 gave selected stress and strain plots for cross-group comparison, showing the respective maximum values. Maximum stress and strain value comparisons showed higher percentage differences. The maximum stress from M5-3 (384 kPa) was 77 and 44 % higher than that from M5-1 (216.2 kPa) and M5-2 (266.6 kPa). It was also 47.9 and 27.5 % higher than that from M1-3 and M3-3. Strain maximum value comparisons were similar to previous ones. Overall, M5 models had higher stress values. Strain values from M5 models were higher than those from M1 and M2 models, but were fairly close to those from M3 and M4 models.
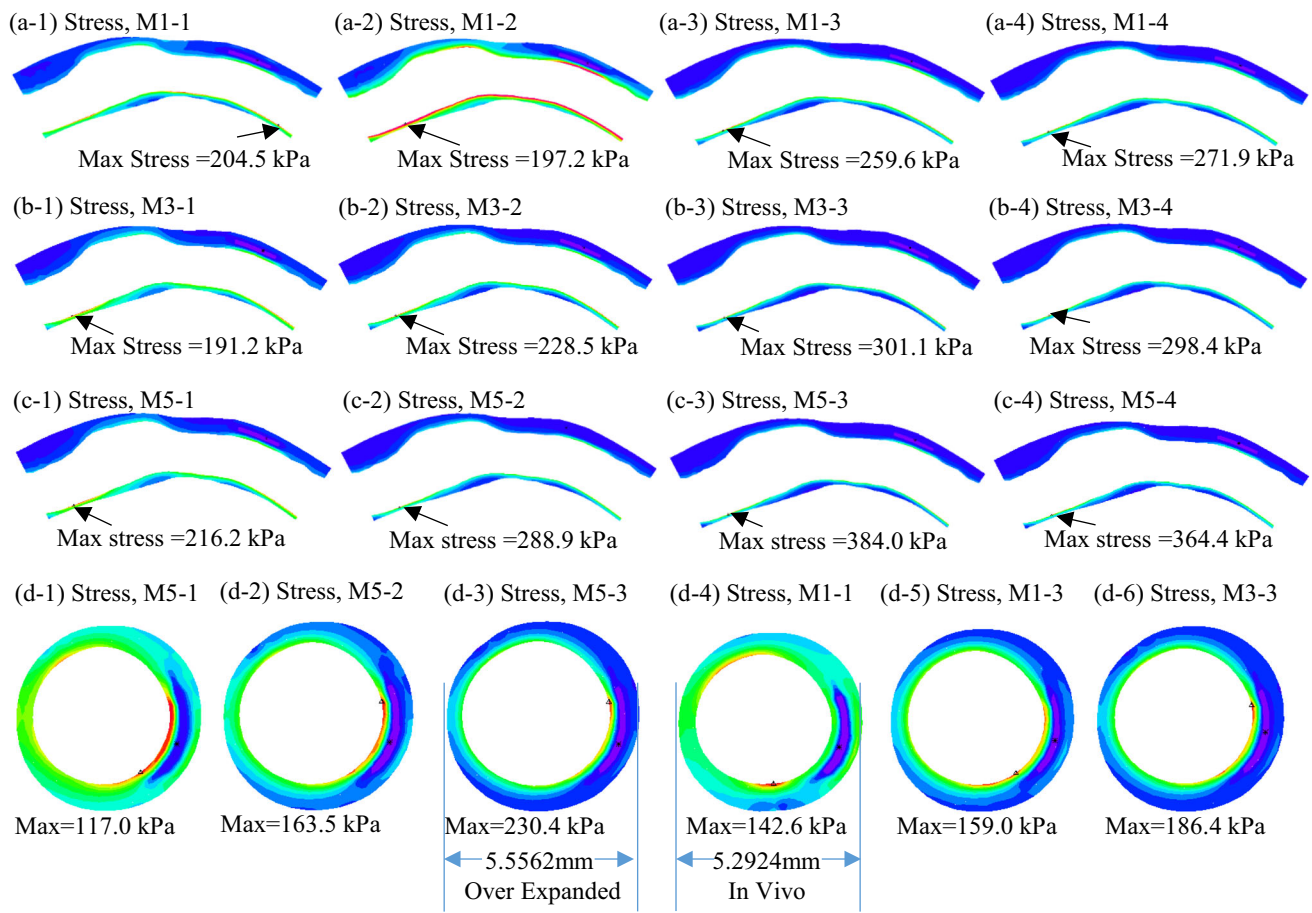
(a-1) Stress, M1-1   (a-2) Stress, M1-2   (a-3) Stress, M1-3   (a-4) Stress, M1-4

Max Stress =204.5 kPa   Max Stress =197.2 kPa   Max Stress =259.6 kPa   Max Stress =271.9 kPa

(b-1) Stress, M3-1   (b-2) Stress, M3-2   (b-3) Stress, M3-3   (b-4) Stress, M3-4

Max Stress =191.2 kPa   Max Stress =228.5 kPa   Max Stress =301.1 kPa   Max Stress =298.4 kPa

(c-1) Stress, M5-1   (c-2) Stress, M5-2   (c-3) Stress, M5-3   (c-4) Stress, M5-4

Max stress =216.2 kPa   Max stress =288.9 kPa   Max stress =384.0 kPa   Max stress =364.4 kPa

(d-1) Stress, M5-1   (d-2) Stress, M5-2   (d-3) Stress, M5-3   (d-4) Stress, M1-1   (d-5) Stress, M1-3   (d-6) Stress, M3-3

Max=117.0 kPa   Max=163.5 kPa   Max=230.4 kPa   Max=142.6 kPa   Max=159.0 kPa   Max=186.4 kPa

5.5562mm   5.2924mm
Over Expanded   In Vivo

Fig. 8 Plaque stress plots from sample M1, M3 and M5 models showing cross-group model comparisons. Selected cross-sectional plots were included. *M1* 5 % axial shrink, adjusted circumferential shrink, *M3* no axial shrink, adjusted circumferential shrink, *M5* no axial shrink, no circumferential shrink

4 Discussion

A Cine IVUS-based thin-wall modeling approach was introduced to obtain patient-specific in vivo vessel material parameter values and circumferential shrinkage rate which are needed for model construction based on in vivo data. This fills a gap in the current literature. Our 3D model results indicate that material parameters have impact on stress and strain calculations. Our results about the material parameter values from Slice 6 and Slice 18 indicated that different locations may have different material parameter values and shrinkages. Axial shrinkage is also an important factor for determining material parameter values.

4.1 The 3D thin-wall modeling to determine vessel material properties is biaxial

Compared to using 2D models in Liu et al. (2012), 3D thin-wall models with 5 % axial stretch were used to match in vivo IVUS data. The 3D thin-wall model is more realistic than 2D models. The 5 % axial stretch rate was used because

the vessel sample has advanced plaque and was relatively stiff, compared to healthy vessels. It was also because it is technically difficult to apply variable axial stretch to a curved vessel. 5 % axial stretch was used in both 3D thin-wall model and the final 3D FSI plaque models.

4.2 Vessel material stiffness has greater impact on strain calculations

Four materials and 5 model groups were simulated in this paper, given 20 models for comparisons. Comparisons could also be made using average lumen, average cap and maximum stress/strain values. Comparing the softest material (S18) with the stiffest material (ex vivo), the 5 modeling experiments indicated that average lumen strain from S18 material was 120–150 % higher than that from the ex vivo material, while the percentages for average lumen stress were around 40–65 %. The average cap strain from S18 material was 150–180 % higher than that from the ex vivo material. The average cap stress from S18 material was 50–75 % higher than that from the ex vivo material. Comparisons between

the S6 and S18 materials could also be made using data from Table 3. It is clear that plaque strain is more sensitive to material stiffness changes.

4.3 Axial and circumferential shrinkages have influence on material stiffness impact

While it is desirable that we could obtain the "accurate and absolutely correct" results, our data and modeling have measurement limitations and modeling simplifications. M1 model group represents the current accepted modeling standard for patient-specific plaque models with plaque components, FSI, curvature, axial and circumferential shrinkages taken into consideration. M1 results indicated that average lumen stress from S18 material was 40% higher than that from the ex vivo material, while the average lumen strain from S18 material was 123% higher than that from the ex vivo material. Dropping axial shrink and stretch process, M3 results showed that average lumen stress from S18 material was 49.5% higher than that from the ex vivo material, while the average lumen strain from S18 material was 169% higher than that from the ex vivo material. Dropping both axial and circumferential shrinkage, the average lumen stress from S18 material was 58% higher than that from the ex vivo material, while the average lumen strain from S18 material was 156% higher than that from the ex vivo material. Models without axial and circumferential shrinkage considerations slightly over-estimated the material stiffness impact.

4.4 Importance of residual stress

As demonstrated by Ohayon et al. (2007), the residual stress has a huge impact on the fibrous cap stress. Ohayon et al. showed that the predicted peak cap stress was about 50 kPa with the residual stress model but could reach 220 kPa using the non-residual stress model (Ohayon et al. 2007). We did our own calculations using idealized geometries, and our results agreed with their findings. Such a huge difference certainly warrants the necessity of considering residual stress in plaque stress analysis. However, an artery segment under *in vivo* condition needs to go through three stages to its open-up shape *ex vivo*: axial shrinkage (percentage unknown and could only estimate), circumferential shrinkage (5–10% based on our data), and final opening-up with an opening angle. Our initial opening angle results from human coronary arteries (mean $\alpha = 120°$, $n = 4$) and carotid arteries (mean $\alpha = 63.5°$, $n = 5$) were reported in (Kural et al. 2012). The axial shrinkage and circumferential shrinkage, which are of equal importance compared to the opening angle step but far less well known, were brought up in our earlier papers (Tang et al. 2008; Yang et al. 2007). The open-up shape is assumed stress-free, which is a well-accepted approximation (even though residual stress still exists if the real physical vessel

ring is cut more). Omitting any of the three stages would lead to stress/strain prediction errors. Our effort in quantifying patient-specific circumferential shrinkage is similar to the effort quantifying open angle addressing the residual stress issue.

We acknowledge that residual stress linked to the opening angle was not included in our current models because it is technically difficult to cut open and wrap up a curved non-uniform patient-specific plaque segment. Relative comparisons of computational stress/strain predictions are still of value in plaque assessment since all patients would be subjected to the same assumptions. Better models would be employed as technology and methods evolve.

Compliance with ethical standards

Conflict of interest There are no conflict of interest to disclose.

References

Barrett SRH, Sutcliffe MPF, Howarth S, Li ZY, Gillard JH (2009) Experimental measurement of the mechanical properties of carotid atherothrombotic plaque fibrous cap. J Biomech 42(11):1650–1655

Bluestein D, Alemu Y, Avrahami I, Gharib M, Dumont K, Ricotta JJ, Einav S (2008) Influence of microcalcifications on vulnerable plaque mechanics using FSI modeling. J Biomech 41(5):1111–1118

Cardoso L, Weinbaum S (2014) Changing views of the biomechanics of vulnerable plaque rupture: a review. Ann Biomed Eng 42(2):415–431

Chai CK, Akyildiz AC, Speelman L, Gijsen FJ, Oomens CW, van Sambeek MR, van der Lugt A, Baaijens FP (2015) Local anisotropic mechanical properties of human carotid atherosclerotic plaques—characterisation by micro-indentation and inverse finite element analysis. J Mech Behav Biomed Mater 43:59–68

Fleg JL, Stone GW, Fayad ZA, Granada JF, Hatsukami TS, Kolodgie FD et al (2012) Detection of high-risk atherosclerotic plaque: report of the NHLBI working group on current status and future directions. JACC Cardiovasc Imaging 5(9):941–955

Friedman MH, Krams R, Chandran KB (2010) Flow interactions with cells and tissues: cardiovascular flows and fluid–structure interactions. Ann Biomed Eng 38(3):1178–87

Fuster V (1998) The vulnerable atherosclerotic plaque: understanding, identification, and modification. In: Fuster V, Cornhill JF, Dinsmore RE, Fallon JT, Insull W, Libby P et al (eds) AHA monograph series. Futura Publishing, Armonk

Gee MW, Reeps C, Eckstein HH, Wall WA (2009) Prestressing in finite deformation abdominal aortic aneurysm simulation. J Biomech 42(11):1732–1739

Holzapfel GA (2000) Nonlinear solid mechanics: a continuum approach for engineering. Wiley, Chichester

Holzapfel GA, Gasser TC, Ogden RW (2000) A new constitutive framework for arterial wall mechanics and a comparative study of material models. J Elast Phys Sci Sol 61(1–3):1–48

Holzapfel GA, Sommer G, Regitnig P (2004) Anisotropic mechanical properties of tissue components in human atherosclerotic plaques. J Biomech Eng 126(5):657–665

Holzapfel GA, Stadler M, Schulze-Bause CAJ (2002) A layer-specific three-dimensional model for the simulation of balloon angioplasty using magnetic resonance imaging and mechanical testing. Ann Biomed Eng 30(6):753–767

Huang X, Yang C, Yuan C, Liu F, Canton G, Zheng J, Woodard PK, Sicard GA, Tang D (2009) Patient-specific artery shrinkage and 3D zero-stress state in multi-component 3D FSI models for carotid atherosclerotic plaques based on in vivo MRI data. Mol Cell Biomech 6(2):121–134

Humphrey JD (2002) Cardiovascular solid mechanics. Springer, New York

Karimi A, Navidbakhsh M, Shojaeic A (2015) A combination of histological analyses and uniaxial tensile tests to determine the material coefficients of the healthy and atherosclerotic human coronary arteries. Tissue Cell 47:152–158

Kural MH, Cai MC, Tang D, Gwyther T, Zheng J, Billiar KL (2012) Planar biaxial characterization of diseased human coronary and carotid arteries for computational modeling. J Biomech 45(5):790–798 (NIHNSID: 344897)

Liu H, Canton G, Yuan C, Yang C, Billiar KL, Teng Z, Hoffman AH, Tang D (2012) Using in vivo Cine and 3D multi-contrast MRI to determine human atherosclerotic carotid artery material properties and circumferential shrinkage rate and their impact on stress/strain predictions. J Biomech Eng 34(1):011008. doi:10.1115/1.4005685

Mintz GS, Nissen SE, Anderson WD, Bailey SR, Erbel R, Fitzgerald PJ, Pinto FJ, Rosenfield K, Siegel RJ, Tuzcu EM, Yock PG (2001) American college of cardiology clinical expert consensus document on standards for acquisition, measurement and reporting of intravascular ultrasound studies (IVUS): a report of the American college of cardiology task force on clinical expert consensus documents. J Am Coll Cardiol 37(5):1478–1492. doi:10.1016/S0735-1097(01)01175-5

Nair A, Kuban BD, Tuzcu EM, Schoenhagen P, Nissen SE, Vince DG (2002) Coronary plaque classification with intravascular ultrasound radiofrequency data analysis. Circulation 106(17):2200–2206. doi:10.1161/01.CIR.0000035654.18341

Nieuwstadt HA, Fekkes S, Hansen HH, de Korte CL, van der Lugt A, Wentzel JJ, van der Steen AF, Gijsen FJ (2015) Carotid plaque elasticity estimation using ultrasound elastography, MRI, and inverse FEA—a numerical feasibility study. Med Eng Phys 37(8):801–807. doi:10.1016/j.medengphy.2015.06.003 (Epub 2015 Jun 27)

Ohayon J, Dubreuil O, Tracqui P, Floc'h SL, Rioufol G, Chalabreysse L, Thivolet F, Pettigrew RI, Finet G (2007) Influence of residual stress/strain on the biomechanical stability of vulnerable coronary plaques: potential impact for evaluating the risk of plaque rupture. Am J Physiol Heart Circ Physiol. 293:H1987–H1996

Pandit A, Lu X, Wang C, Kassab GS (2005) Biaxial elastic material properties of porcine coronary media and adventitia. Am J Physiol Heart Circ Physiol 288(6):H2581–H2587

Samady H, Eshtehardi P, McDaniel MC, Suo J, Dhawan SS, Maynard C, Timmins LH, Quyyumi AA, Giddens DP (2011) Coronary artery wall shear stress is associated with progression and transformation of atherosclerotic plaque and arterial remodeling in patients with coronary artery disease. Circulation 124(7):779–788

Speelman L, Akyildiz AC, Den Adel B, Wentzel JJ, Van der Steen AF, Virmani R, Van der Weerd L, Jukema JW, Poelmann RE, Van Brummelen EH, Gijsen FJ (2011) Initial stress in biomechanical models of atherosclerotic plaques. J Biomech 44(13):2376–2382

Stary HC, Chandler AB, Dinsmore RE, Fuster V, Glagov S, Insull W Jr, Rosenfeld ME, Schwartz CJ, Wagner WD, Wissler RW (1995) A definition of advanced types of atherosclerotic lesions and the histological classification of atherosclerosis. A report from the Committee on Vascular Lesions of the Council on Arteriosclerosis, AHA. Circulation 92:1355–1374

Stone PH, Saito S, Takahashi S, Makita Y, Nakamura S, Kawasaki T, Takahashi A, Katsuki T, Nakamura S, Namiki A, Hirohata A, Matsumura T, Yamazaki S, Yokoi H, Tanaka S, Otsuji S, Yoshimach F, Honye J, Harwood D, Reitman M, Coskun AU, Papafaklis MI, Feldman CL (2012) PREDICTION Investigators. Prediction of progression of coronary artery disease and clinical outcomes using vascular profiling of endothelial shear stress and arterial plaque characteristics: the PREDICTION Study. Circulation 126(2):172–181

Tang D, Kamm RD, Yang C, Zheng J, Canton G, Bach RG et al (2014) Image-based modeling for better understanding and assessment of atherosclerotic plaque progression and vulnerability: data, modeling, validation, uncertainty and predictions. J Biomech 47(4):834–846

Tang D, Teng Z, Canton G, Yang C, Ferguson M, Huang X, Zheng J, Woodard PK, Yuan C (2009) Sites of rupture in human atherosclerotic carotid plaques are associated with high structural stresses. An in vivo MRI-based 3D fluid–structure interaction study. Stroke. 40:3258–3263 (Featured article on MDlinx.com)

Tang D, Yang C, Mondal S, Liu F, Canton G, Hatsukami TS, Yuan C (2008) A negative correlation between human carotid atherosclerotic plaque progression and plaque wall stress: in vivo MRI-based 2D/3D FSI models. J Biomech 41(4):727–736 (Featured article by the Society for Heart Attack Prevention and Eradication (SHAPE), 2008)

Teng Z, Tang D, Zheng J, Woodard PK, Hoffman AH (2009) An experimental study on the ultimate strength of the adventitia and media of human atherosclerotic carotid arteries in circumferential and axial directions. J Biomech 42(15):2535–2539

Teng Z, Zhang Y, Huang Y, Feng J, Yuan J, Lu Q, Sutcliffe MP, Brown AJ, Jing Z, Gillard JH (2014) Material properties of components in human carotid atherosclerotic plaques: a uniaxial extension study. Acta Biomater S1742–7061(14):00379-1

Walsh MT, Cunnane EM, Mulvihill JJ, Akyildiz AC, Gijsen FJ, Holzapfel GA (2014) Uniaxial tensile testing approaches for characterization of atherosclerotic plaques. J Biomech 47(4):793–804. doi:10.1016/j.jbiomech.2014.01.017 (Epub 2014 Jan 14)

Wang L, Zheng J, Maehara A, Yang C, Billiar KL, Wu Z, Bach R, Muccigrosso D, Mintz GS, Tang D (2015) Morphological and stress vulnerability indices for human coronary plaques and their correlations with cap thickness and lipid percent: an IVUS-based fluid–structure interaction multi-patient study. PLoS Comput Biol 11(12):e1004652. doi:10.1371/journal.pcbi.1004652

Yang C, Bach R, Zheng J, El Naqa I, Woodard PK, Teng Z, Billiar KL, Tang D (2009) In vivo IVUS-based 3D fluid structure interaction models with cyclic bending and anisotropic vessel properties for human atherosclerotic coronary plaque mechanical analysis. IEEE Trans Biomed Eng 56(10):2420–2428

Yang C, Tang D, Yuan C, Hatsukami TS, Zheng J, Woodard PK (2007) In vivo/ ex vivo MRI-based 3D models with fluid–structure interactions for human atherosclerotic plaques compared with fluid/wall-only models. CMES Comput Model Eng Sci 19(3):233–245